Impact-generated dust clouds around planetary satellites: asymmetry effects

Miodrag Sremčević[*], Alexander V. Krivov[1], Frank Spahn

AG "Nichtlineare Dynamik", Institut für Physik, Universität Potsdam, Postfach 601553, 14415 Potsdam, Germany

Abstract

In a companion paper (Krivov et al., Impact-generated dust clouds around planetary satellites: spherically symmetric case, Planet. Space. Sci. 2003, 51, 251–269) an analytic model of an impact-generated, steady-state, spherically symmetric dust cloud around an atmosphereless planetary satellite (or planet—Mercury, Pluto) has been developed. This paper lifts the assumption of spherical symmetry and focuses on the asymmetry effects that result from the motion of the parent body through an isotropic field of impactors. As in the spherically symmetric case, we first consider the dust production from the surface and then derive a general phase-space distribution function of the ensemble of ejected dust motes. All quantities of interest, such as particle number densities and fluxes, can be obtained by integrating this phase-space distribution function.

As an example, we calculate an asymmetric distribution of dust number density in a cloud. It is found that the deviation from the symmetric case can be accurately described by a cosine function of the colatitude measured from the apex of the satellite motion. This property of the asymmetry is rather robust. It is shown that even an extremely asymmetric dust production at the surface, when nearly all dust is ejected from the leading hemisphere, turns rapidly into the cosine modulation of the number density at distances larger than a few satellite radii. The amplitude of the modulation depends on the ratio of the moon orbital velocity to the speed of impactors and on the initial angular distribution of the ejecta. Furthermore, regardless of the functional form of the initial angular distribution, the number density distribution of the dust cloud is only sensitive to the mean ejecta angle. When the mean angle is small—ejection close to the normal of the surface—the initial dust production asymmetry remains persistent even far from the satellite, but when this angle is larger than about 45°, the asymmetry coefficient drops very rapidly with the increasing distance. The dependence of the asymmetric number density on other parameters is very weak.

On the whole, our results provide necessary theoretical guidelines for a dedicated quest of asymmetries in the dust detector data, both those obtained by the Galileo dust detector around the Galilean satellites of Jupiter and those expected from the Cassini dust experiment around outer Saturnian moons.

1. Introduction

Atmosphereless celestial objects are subject to continuous bombardment by hypervelocity micrometeoroids. These energetic impacts produce secondary dust which is kicked off the surface, and this impact ejection process has been suggested as the main source of Jovian dusty rings (Morfill et al., 1980), a very tenuous ring between the Galilean satellites of

Jupiter (Krivov et al., 2002), Saturn's E ring (Horányi et al., 1992), as well as of possible dust envelopes of Mars (Soter, 1971; Krivov and Hamilton, 1997; Krivov and Jurewicz, 1999), Pluto and Charon (Thiessenhusen et al., 2002), Mercury (Müller et al., 2002), asteroids and Kuiper belt objects. The subject of this study are tenuous impact-generated dust envelopes of planetary satellites. This class of objects has recently been discovered through an analysis of in-situ measurements made by the Galileo spacecraft in the Jovian system (Krüger et al., 1999, 2000, 2003). As yet, clouds are only known to exist around four specific moons of Jupiter—Io, Europa, Ganymede, and Callisto. Their extremely low optical depth rules out remote sensing, and the only way to discover and measure them is to perform in-situ

---

[*] Corresponding author. Tel.: +49-331-977-1131; fax: +49-331-977-1142.

E-mail address: msremac@agnld.uni-potsdam.de (M. Sremčević).

[1] On leave from: Astronomical Institute, St. Petersburg University, Russia.

measurements by dust detectors aboard space missions. Future numerous flybys of Saturnian satellites by the Cassini spacecraft, dust measurements near Phobos and Deimos by the Nozomi spacecraft and a dust experiment at Mercury by the BepiColombo mission offer new opportunities to reveal and study ethereal dust envelopes.

Our study conceptually continues on works of Cuzzi and Durisen (1990) and Colwell (1993). They carefully modelled different families of dust impactors and obtained the distribution of ejected dust leaving the satellite system. Part of their calculations was done assuming the far-field approximation. However, the Galileo spacecraft detected the dust particles in close vicinities of Jovian moons, up to 10 of satellite radii, and in these ranges the previous description would require extensive numerical calculations (Spahn et al., 1999). Thus, we were motivated to develop a model that would give the dust distribution close to the moon surface in an analytic form. The model considers only the gravity of the moon and is valid within the Hill sphere radius. This permits an analytic solution and a unified description of all dust envelopes around planetary satellites. Our analytic solution allows an easy incorporation of different dust production models and a future goal would be to straighten out plausible scenarios and production parameters comparing model predictions and in-situ measurements. Here we focus on applications to Jovian and Saturnian moons, having in mind available Galileo dust data and future Cassini mission data.

In a companion paper (Krivov et al. (2003), hereinafter referred to as PAPER I) we developed an analytic model of a steady-state, spherically symmetric dust cloud around an atmosphereless body, maintained by impacts of interplanetary micrometeoroids. Of all the assumptions made in PAPER I, the one of spherical symmetry is perhaps the most severe. Although many of the satellites are nearly spherical in shape, substantial asymmetries can be expected from the orbital motion of the parent body through an isotropic field of impactors. Here we lift the assumption of spherical symmetry and concentrate on these asymmetry effects.

This paper is conceptually very close to PAPER I and is essentially based on the results presented there. The key concept of our approach is the phase-space DF (distribution function), which is the most general quantity describing the dust population. The derivation of the phase-space DF is based on the transformation of the phase-space variables at the satellite surface along the dust particle trajectories, for a given initial distribution of ejecta from the surface. Once derived, the phase-space DF allows computation of all quantities of interest, such as the number density of dust at different points around a moon or the dust fluxes onto a detector flying near the satellite.

As in PAPER I, we first consider the dust production from the surface (Section 2), describing it with a DF. We add a spatial dependence on the point at the moon surface by using a convenient parameterization. In Section 3, we derive an expression for the phase-space DF, valid for any dust production law at the surface. The reader not interested in technical details may want to skip much of Sections 2.2, 2.3, 3.2 and 3.3 and to proceed to Section 4, where we calculate the number density. This is done using the parameterization of the dust production and integrating the zeroth moment of the phase-space DF. We also discuss the influence of different parameters and models of the dust production on the number density. Essential parameters are identified and numerical examples for specific satellites are given. In Section 5, we summarize our findings.

2. Asymmetric dust production

2.1. Assumptions

Consider the following model for the velocity field of the impacting micrometeoroids (interplanetary dust particles, or IDPs). We assume that: (i) all the impactors have the same speed v_{IDPs} with respect to an *inertial reference frame* (with respect to the Sun), and (ii) the velocity vectors are distributed isotropically, in the same inertial reference frame.

The first of these assumptions can be taken without loss of generality. For an arbitrary distribution of the velocity moduli, the results can be obtained simply by summing (integrating) the "monospeed" results we are going to obtain. Plausibility of the second assumption is not easy to verify, given the poor knowledge of the interplanetary dust environment. However, general arguments that may be used in one or another system suggest that the assumption is reasonable. For instance, at Jupiter and Saturn much of the interplanetary matter is thought to come from long-period comets. This dust population, also termed "Oort cloud" population (Colwell and Horányi, 1996), consists of particles with highly eccentric, but randomly inclined orbits—albeit another, "planetary" population of micrometeoroids in low-eccentricity, low-inclination orbits presumably coming from the Edgeworth–Kuiper belt might be of importance in the outer solar system. In comparison, Divine's (1993) model, based on the spacecraft dust detector data, indicates that the dust environment at Jupiter and especially Saturn is dominated by a "halo population", characterized by moderate eccentricities, but broadly distributed inclinations. Due to a very broad distribution of inclinations, both the Oort cloud and halo populations are compatible with the isotropy assumption we made.

In the case of Jupiter, simple estimates (see Paper I) give the velocities of the Oort cloud population impactors in the range from 4 to 24 km s^{-1}, with typical values of about 20 km s^{-1}. After taking into account gravitational focussing of the impactor flux by the planet, typical speeds increase to about 25 km s^{-1} (Krüger et al., 2000). This value is a typical speed of the projectiles with respect to the Sun (i.e. in the inertial frame of reference) at the satellite location. It is comparable with both orbital velocities of planets relative to the Sun (13.1 km s^{-1} for Jupiter) and the orbital

velocities of the satellites. For instance, the velocities of Callisto, Ganymede, and Europa are 8.2, 10.9, and 13.7 km s^{-1}, respectively. As a result, the velocity v_{moon} of the satellite in the inertial frame may be of the same order of magnitude as the impactors speed in the same frame, v_{IDPs}. The velocities of the impactors with respect to the satellite, $\vec{v}_{\text{imp}} \equiv \vec{v}_{\text{IDPs}} - \vec{v}_{\text{moon}}$, will be quite diverse at different surface points and for distinct positions of the moon on its orbit. Therefore, a substantial anisotropy of impactor fluxes on the moons surfaces is expected (e.g. Colwell, 1993; Spahn et al., 1999).

A quantitative example is given by Krüger et al. (2000) for the Jovian moon Ganymede. Considering the geometry of the orbital motions of Jupiter, Ganymede, and IDPs, it is easy to show that velocities of the grains with respect to Ganymede vary from nearly zero to about 50 km s^{-1}, depending on the position of Ganymede on its orbit and the directions of the particle velocities. These extreme velocity values are attained when Ganymede is at opposition to the Sun, at which moment we can expect a very high asymmetry of the dust cloud above the leading and trailing hemispheres of the moon. The effect gets much smaller at Ganymede's conjunction, when the prograde particles hit the trailing hemisphere with $\geqslant 23$ and retrograde grains reach the leading side with $\leqslant 27$ km s^{-1}, but still many more impacts are expected on the leading edge of Ganymede than on the trailing edge.

In the following we assume that the asymmetry is caused only by the motion of the parent body through the cloud of "mono-speed" IDPs with isotropically distributed velocity vectors. This is modelled by the spatially dependent dust production, while for the initial velocities of the ejected dust grains we follow PAPER I (cf. Section 2.4). In fact, this means that dust is produced in the same way, but now the dust production rate depends on the spatial location at the satellite surface. This is not exactly true, but our model covers the main reason for the asymmetry. Another point is that parameters of the dust production can be very uncertain. However, the dust distribution is addressed in a very general way, and any improvement of the dust production model can be incorporated directly through corresponding parameters.

2.2. Dust production rate

Consider a spherical coordinate system fixed at the center of the parent moon with Z-axis pointing in the direction of the velocity vector of the moon $\vec{v}_{\text{moon}}$ (apex). Then, the colatitude α_M and the longitude β_M characterize the impact site at the surface of the satellite (Fig. 1). The velocities of the impactors will be referred to the inertial spherical coordinate system, where α_{imp} and β_{imp} are the colatitude (cone angle) and the longitude (clock angle) of the velocity vector, respectively. Please refer to Table 1 for a list of variables frequently used in this paper.
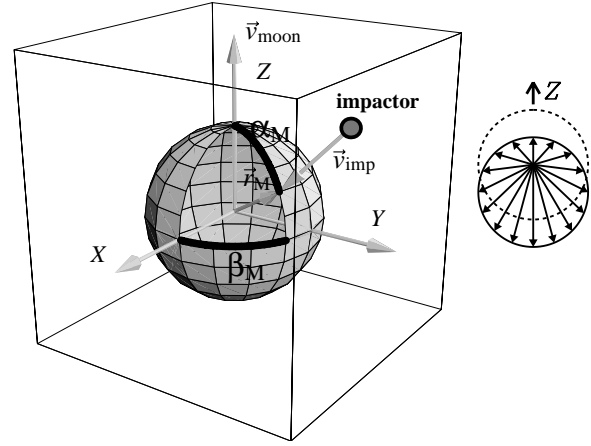

Fig. 1. (Left) Geometry of micrometeoroidal bombardment of the surface of a spherically symmetric satellite. The XZ plane coincides with the equatorial plane. (Right) Velocities (in a plane) of mono-speed impactors in the satellite-fixed coordinate system. Impactors with such velocities (the ones with $\vec{r}_M \cdot \vec{v}_{\text{imp}} \leqslant 0$) strike each point of the surface. The dashed line represents the isotropic motionless case ($\vec{v}_{\text{moon}} = 0$).

The radius vector of the impact point and the velocity vector of an impactor can be written as

$$\vec{r}_M = r_M(\sin \alpha_M \cos \beta_M, \; \sin \alpha_M \sin \beta_M, \; \cos \alpha_M), \tag{1}$$

$$\vec{v}_{\text{imp}} = v_{\text{IDPs}}(\sin \alpha_{\text{imp}} \cos \beta_{\text{imp}}, \sin \alpha_{\text{imp}} \sin \beta_{\text{imp}},$$
$$\cos \alpha_{\text{imp}} - \mu), \tag{2}$$

with $\mu \equiv v_{\text{moon}}/v_{\text{IDPs}}$, where v_{moon} and v_{IDPs} are the speeds of the parent moon and the impactors, respectively. The impactors approach the impact point from the hemisphere above the local horizon, implying the condition

$$\vec{r}_M \cdot \vec{v}_{\text{imp}}/(r_M v_{\text{imp}}) = \cos(\vec{r}_M, \vec{v}_{\text{imp}}) \leqslant 0. \tag{3}$$

Thus the angles α_{imp} and β_{imp} must fall into the domain

$$D(\alpha_M, \beta_M) \equiv \{\alpha_{\text{imp}}, \beta_{\text{imp}} \mid \sin \alpha_M \sin \alpha_{\text{imp}} \cos(\beta_{\text{imp}} - \beta_M)$$
$$+ \cos \alpha_M(\cos \alpha_{\text{imp}} - \mu) \leqslant 0\}. \tag{4}$$

We now consider the dust production at different points of the surface. Denote by P the dust production rate per unit area at the impact site (α_M, β_M). Because of the assumed rotational symmetry with respect to the Z-axis, neither $P(\alpha_M)$ nor v_{imp} depend on the longitude β_M. Of course, this angle enters the expression for the domain D via $\beta_{\text{imp}} - \beta_M$, but since the clock angle β_M is uniformly distributed, β_M is of no interest. The dust production rate varies as $P(\alpha_M) \propto F_{\text{imp}}(v_{\text{imp}}) \times Y(v_{\text{imp}}) \times \cos(\vec{r}_M, -\vec{v}_{\text{imp}})$ with the impactor flux $F_{\text{imp}} \propto v_{\text{imp}}$ and the characteristic yield $Y \propto v_{\text{imp}}^{2b}$. The cosine term results from the projection of the surface target area. Experimental data from Koschny and Grün (2001a) for ice-silicate mixtures as targets suggest the value $b = 1.23$. However, keeping in mind large uncertainties of all quantities characterizing the impact ejection processes, we use the

Table 1
Nomenclature

Symbol	Definition
v_{IDPs}	mass-weighted average speed of impactors in the inertial frame
$\vec{v}_{moon}$ (v_{moon})	instantaneous satellite velocity (speed) in the inertial frame
$\vec{v}_{imp}$ (v_{imp})	velocity (speed) of impactors in the *satellite* reference frame
α_{imp} (β_{imp})	colatitude (clock angle) of impactor velocity in the *inertial* reference frame.
μ	Direction $\alpha_{imp} = 0$ coincides with direction $\vec{v}_{moon}$ scaled satellite velocity $\mu = v_{moon}/v_{IDPs}$
$\vec{r}_M$ (r_M)	radius vector of a point on the satellite surface (satellite radius)
α_M (β_M)	colatitude (longitude) of a point on the satellite surface measured from the
$\vec{u}$ (u)	apex of the motion, Figs. 1 and 4 ejecta velocity (speed)
ψ	angle between ejecta velocity $\vec{u}$ and surface radius vector $\vec{r}_M$, Fig. 4
λ_M	clock angle of ejecta velocity $\vec{u}$ measured from the apex, Fig. 4
$\vec{r}$ (r)	radius vector (distance) of a point in space
α (β)	colatitude (longitude) of $\vec{r}$ measured from the apex of the motion, Fig. 4
$\vec{v}$ (v)	velocity (speed) of dust grain at $\vec{r}$, Fig. 4
θ	angle between the velocity $\vec{v}$ and radius vector $\vec{r}$, Fig. 4
λ	clock angle of velocity $\vec{v}$ measured from the apex, Fig. 4
$v_{esc}(M_{moon})$	surface escape velocity (mass of the moon)
$\Delta\phi$	angle between $\vec{r}_M$ and $\vec{r}$, Fig. 4

widely accepted value of $b = 1$ in order to keep the calculations as simple as possible. Physically, this means that the amount of the ejected material is controlled essentially by the kinetic energy of the impactors.

Then, by summing over the solid angle $d\Omega(\alpha_{imp}, \beta_{imp}) \equiv \sin\alpha_{imp} \, d\alpha_{imp} \, d\beta_{imp}$ we finally obtain the production rate as a function of the colatitude α_M

$$P(\alpha_M) = \text{const} \int_{D(\alpha_M,\beta_M)} v_{imp}^{2b+1}(\alpha_{imp}, \beta_{imp})$$
$$\times \cos(\vec{r}_M, -\vec{v}_{imp}) \, d\Omega(\alpha_{imp}, \beta_{imp}). \quad (5)$$

The production rate of a motionless satellite $v_{moon} = 0 (v_{imp} = v_{IDPs})$ will serve as a reference value:

$$P_0 = \text{const} \int_{2\pi} v_{IDPs}^{2b+1} \cos(\vec{r}_M, -\vec{v}_{imp}) \, d\Omega(\alpha_{imp}, \beta_{imp})$$
$$= \text{const} \, \pi v_{IDPs}^{2b+1}. \quad (6)$$

Physically, P_0 is the dust production rate per unit surface area which is steadily sustained by the impactors that arrive from a solid angle of 2π and hit the surface with the speed v_{IDPs} (factor π results from the projection). It is equal to

$$P_0 \equiv \frac{N^+}{4\pi r_M^2}, \quad (7)$$

where N^+ is the total number of dust grains ejected from the whole surface of the motionless moon per unit time (see PAPER I).

Another quantity of interest is the solid angle Ω subtended by the velocity vector of impactors that are able to reach the surface at a given colatitude α_M:

$$\Omega(\alpha_M) \equiv \int_{D(\alpha_M,\beta_M)} d\Omega(\alpha_{imp}, \beta_{imp}). \quad (8)$$

All integrals are analytically solvable and the calculations are given in Appendix A.

In Fig. 2 (top) the dust production $P(\alpha_M)$ normalized to unity (with geometrical weight $\sin\alpha_M$) is plotted as a function of α_M (for $b = 1$) for several values of μ. Fig. 2 (bottom) depicts the solid angle $\Omega(\alpha_M)$. It shows that more IDPs hit the leading hemisphere than the trailing one if the satellite is moving ($v_{moon} > 0$). The faster the moon moves (the larger μ), the more pronounced the effect. In addition to this, the impactor velocities are larger at the leading hemisphere than at the trailing one. In total this gives a considerable rise of the dust production near the apex, and a decrease at the opposite pole compared to the motionless case. When $\mu = 1$, the trailing pole becomes almost unreachable by impactors. It is worth noting that our profiles $P(\alpha_M)$ resemble the ejecta profiles by Cuzzi and Durisen (1990) and Colwell (1993), although the latter are scattering functions of the whole parent body at large distances from it.

2.3. Ejecta distribution

The number of particles ejected from the belt at the surface of the satellite $[\alpha_M, \alpha_M + d\alpha_M]$, having velocities $\vec{u}(u, \psi, \lambda_M)$ in the interval $du \, d\psi \, d\lambda_M$ and during the time dt is

$$dn = N^+ B \, dt \, f(\alpha_M, u, \psi, \lambda_M) \, d\alpha_M \, du \, d\psi \, d\lambda_M. \quad (9)$$

Here $N^+ B$ is the total number of particles ejected from the whole surface of the moon per unit time. The dimensionless parameter $B(\mu)$ reflects the increase of the production due to the motion of the satellite so that f is normalized to unity. The angles λ_M and ψ determine the direction of the ejecta velocity $\vec{u}(u, \psi, \lambda_M)$. The angle ψ is the velocity colatitude (cone angle) measured from the normal of the surface ($\vec{r}_M$), whereas λ_M denotes a clock angle measured from the apex.
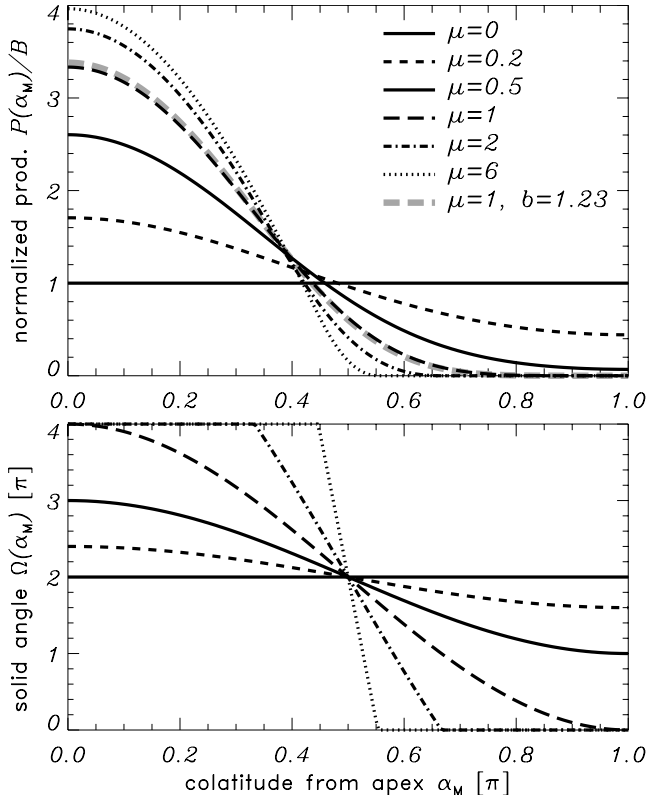
Fig. 2. Anisotropy of the dust production. Top: The dust production $P(\alpha_M)$, Eq. (A.2), normalized to unity with a geometrical weight $\sin \alpha_M$ is plotted for different μ (for $b = 1$). Taking $b = 1.23$ does not give any significant difference (gray dashed line). Bottom: The solid angle $\Omega(\alpha_M)$ subtended by the velocity vectors of impactors (in inertial frame) that can hit a given point at the surface of the satellite (Eq. (8)). The larger the relative orbital velocity of the satellite μ, the more impactors are hitting the leading hemisphere ($\alpha_M \leqslant \pi/2$).

Formal definitions of these angles are

$$\psi = \sphericalangle(\vec{r}_M, \vec{u}), \qquad \lambda_M = \sphericalangle(\vec{v}_{moon}^\perp, \vec{u}^\perp),$$

$$\vec{u}^\perp \cdot \vec{r}_M = \vec{v}_{moon}^\perp \cdot \vec{r}_M = 0. \tag{10}$$

The fact that $\vec{u}$ has to point outward from the surface of the moon leads to the interval $\psi \in [0, \pi/2]$, and we assume additional reflectional symmetry $f(\lambda_M) = f(-\lambda_M)$ so that $\lambda_M \in [0, \pi]$.

The ejecta DF $f(\alpha_M, u, \psi, \lambda_M)$ is normalized to unity, according to

$$\int_0^\pi \mathrm{d}\alpha_M \int_0^\infty \mathrm{d}u \int_0^{\pi/2} \mathrm{d}\psi \int_0^\pi \mathrm{d}\lambda_M f(\alpha_M, u, \psi, \lambda_M) = 1. \tag{11}$$

The choice of normalization to $\mathrm{d}\alpha_M \, \mathrm{d}u \, \mathrm{d}\psi \, \mathrm{d}\lambda_M$ rather than to the geometrical unit volume (i.e. $\sin \alpha_M \, \mathrm{d}\alpha_M u^2 \, \mathrm{d}u \sin \psi \, \mathrm{d}\psi \, \mathrm{d}\lambda_M$) is mainly to favor an easy formulation of the distribution of the speed $f_u(u)$ (see below).

Unless otherwise stated, we will factorize the ejecta DF and write

$$f(\alpha_M, u, \psi, \lambda_M) = f_\alpha(\alpha_M) f_u(u) f_\psi(\psi) f_\lambda(\lambda_M), \tag{12}$$

thereby assuming a statistical independence of the factors in Eq. (12). Each factor has to be normalized to unity again. Using the dust production rate $P(\alpha_M)$ and taking into account the normalization, we obtain

$$f_\alpha(\alpha_M) = \frac{\sin \alpha_M}{2} \frac{P(\alpha_M)}{B},$$

$$B(\mu) = \int_0^\pi \mathrm{d}\alpha_M \frac{\sin \alpha_M}{2} P(\alpha_M). \tag{13}$$

Here, the term $\sin \alpha_M$ comes from the geometrical unit volume [because of the normalization (11)].

For the further calculation we will expand $f_\alpha(\alpha_M)$ into the Legendre polynomials $\mathbf{P}_n$ of $\cos \alpha_M$ (spherical harmonics Y_n^0). This is done because of the geometry of the problem. Additionally, any further improvement of the impact ejection process model can be easily incorporated through coefficients of the Legendre polynomials:

$$f_\alpha(\alpha_M) = \frac{\sin \alpha_M}{2} \left[1 + C^{(1)} \mathbf{P}_1(\alpha_M) \right.$$

$$\left. + C^{(2)} \mathbf{P}_2(\alpha_M) + \cdots \right]. \tag{14}$$

We use an abbreviation $\mathbf{P}_n(\alpha) \equiv \mathbf{P}_n[\cos \alpha]$, and the first few polynomials are (Gradshteyn and Ryzhik, 1994): $\mathbf{P}_0(\alpha) = 1$, $\mathbf{P}_1(\alpha) = \cos \alpha$, $\mathbf{P}_2(\alpha) = (3 \cos^2 \alpha - 1)/2$, etc. The polynomials are orthogonal with the weight $\sin \alpha$, and in this view $B(\mu)$ is the zeroth coefficient of $P(\alpha_M)$, while other coefficients are calculated as

$$C^{(n)}(\mu) = \frac{2n+1}{2} \int_0^\pi \frac{P(\alpha_M)}{B} \mathbf{P}_n(\alpha_M) \sin \alpha_M \, \mathrm{d}\alpha_M. \tag{15}$$

Using Eq. (A.1) for $P(\alpha_M)$ from Appendix A we get

$$B(\mu) = 1 + 2\mu^2 + \mu^4/5,$$

$$C^{(1)}(\mu) = 2\mu(5/3 + \mu^2)/B(\mu),$$

$$C^{(2)}(\mu) = 2\mu^2(1 + \mu^2/7)/B(\mu),$$

$$C^{(3)}(\mu) = 0. \tag{16}$$

Other coefficients are either 0 or very small. The above expressions are strictly valid for $\mu \leqslant 1$, but they are nearly exact for μ values that we need: $\mu < 2$.

Fig. 3. displays the functional dependence of coefficients $B(\mu)$ and $C^{(n)}(\mu)$. As can be seen from Fig. 3, the choice of the power-law exponent $b = 1.23$ for the characteristic yield $Y \propto v_{imp}^{2b}$ does not bring any significant difference. The shape of the production rate $P(\alpha_M)/B(\mu)$ and the coefficients $C^{(n)}(\mu)$ remain the same within 1% of the value for $b = 1$; only the scaling factor $B(\mu)$ slightly increases for larger μ.

2.4. Initial velocity distribution

The distribution of the initial velocities $\vec{u}$ of ejected dust grains from the surface of the satellite is discussed in great detail in PAPER I. Here we briefly reproduce the
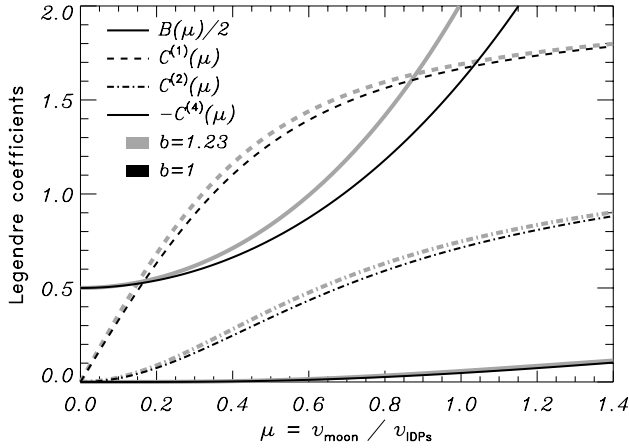
Fig. 3. Coefficients $B(\mu)$ and $C^{(n)}(\mu)$ of the dust production $P(\alpha_M)$ expansion into Legendre polynomials as functions of the scaled satellite velocity μ. The coefficient $C^{(3)} = 0$. Black lines stand for the yield exponent $b = 1$, Eqs. (16), while thick gray lines denote numerically obtained values for $b = 1.23$.

presumptions. The distribution functions are postulated, and this choice should be considered as a "canonical" case.

The moduli of initial velocities u are postulated to be

$$f_u(u) = \frac{\gamma}{u_0} \left(\frac{u}{u_0} \right)^{-\gamma-1} H[u - u_0]. \tag{17}$$

The coefficient $-\gamma$ is the slope of the cumulative distribution, u_0 is the lower limit of the velocities, and $H[z]$ is the Heaviside step function.

We assume that grains are ejected isotropically within a cone with the opening angle ψ_0

$$f_\psi(\psi) = \frac{\sin \psi}{1 - \cos \psi_0} H[\psi_0 - \psi]. \tag{18}$$

The clock angles λ_M are taken to be uniformly distributed (in range $[0, \pi]$) : $f_\lambda(\lambda_M) = 1/\pi$, so that there is no preferred ejecta direction in the tangential plane of the surface.

In Table 2 we list, for several Jovian and Saturnian satellites, the following quantities: Hill sphere radius h, the mass-weighted average velocities of impactors v_{IDPs}, the coefficients N^+, u_0 and γ of the ejecta DF, the orbital speed of the moons v_{orb}, as well as the range of the scaled moon speed μ. The list of satellites includes Io, Europa, Ganymede and Callisto, the dust clouds around which have been discovered during the dust experiment aboard the Galileo spacecraft; Amalthea, flown by Galileo in November 2002; and several satellites of Saturn, as yet undiscovered dust clouds of which are probable targets for the dust experiment aboard the Cassini spacecraft. Most of the data collected in the table are reproduced from PAPER I, to which the reader is referred for further explanations. Here we only note that the values of N^+ represent the production rates of grains with masses greater than the detector threshold of Galileo (Jovian moons) and Cassini (Saturnian satellites). In turn, the threshold, which depends on the impact velocities of the cloud grains onto the detector, was computed for particular

flybys, the parameters of which can also be found in PAPER I. The last three columns in Table 2 are new and contain parameters related to the orbital motion of the moons and therefore responsible for the expected asymmetries of the clouds.

2.5. Seasonal variations

The most crucial assumption of our further calculations is stationarity of the dust population which, in turn, implies that (i) the impactor flux is stationary and (ii) given the flux of impactors, the dust production does not depend on time. The first assumption is a good approximation to reality, as long as impactors are considered to be interplanetary micrometeoroids, whereas short-lasting events such as impacts of larger meteorites or occasional crossings of meteor swarms are neglected. A violation of the second assumption can be caused by time variability of the impactor speed, owing to the orbital motions of the involved bodies. To check the validity of the second assumption, we can compare time-spans of ejected dust grains in clouds τ and orbital periods of satellites T_{moon}. As a characteristic timescale τ, we choose one-half of the orbital period of the dust particles with the semimajor axis $a = 3r_M$ (for escaping particles and ones with $a < 3r_M$ this time is shorter). These grains significantly contribute to the region from 3 to 6 satellite radii. For satellites listed in Table 2, we find τ to be about 6 –8 h. Compared to the orbital periods of satellites, we have the typical situation at Ganymede where $\tau = 6$ h against $T_{moon} = 7.1$ days. The worst situation is at Enceladus where $\tau = 8$ h and $T_{moon} = 1.4$ days. Nevertheless, $\tau \ll T_{moon}$.

Our model considers only the gravity of the moon and is valid within the Hill sphere radius (Table 2). It should be kept in mind that in some cases electro-magnetic forces might not be negligible, as the grains can quickly collect charges in the photoelectron sheath around the sunlit side of the satellite, and respond to the electric field present in the photoelectron sheath. This may change the dynamics, generating beside bound back-falling ejecta and unbound escaping ejecta also bound ejecta orbiting the moon, dust levitation above the surface, dusk/dawn asymmetry, etc. These potentially interesting effects are beyond the scope of this paper. Other forces, such as the gravity of the planet, inertial forces, and radiation pressure become important over longer time spans, i.e. in orbit around the planet, and thus, far from the parent satellite (Krivov and Jurewicz, 1999; Spahn et al., 1999).

From here on we assume stationarity, but in applications of the results, the coefficients $B(\mu)$ and $C(\mu)$ are taken according to the satellite position on its orbit around the planet, or in other words we consider formation of clouds to be adiabatic. Therefore, $\mu = v_{moon}/v_{IDPs}$ and Z-axis coincides with $\vec{v}_{moon}$, where $\vec{v}_{moon}$ is the *instantaneous* velocity of the moon in the inertial frame of reference (with respect to the Sun). In Table 2, we display the minimum and maximum

Table 2
Model parameters for different Jovian and Saturnian satellites: Hill sphere radius h in the moon radii, speed of impactors v_{IDPs}, ejecta speed distribution parameters u_0 and γ, number of ejected grains with masses above the detector threshold per unit time N^+ (flyby-dependent), orbital velocity of the moon v_{orb}, and limits of the scaled moon velocity μ_{min} and μ_{max}

Satellite (Flyby)	h/r_M	v_{IDPs} (km s^{-1})	u_0 (m s^{-1})	γ	N^+ (s^{-1})	v_{orb} (km s^{-1})	μ_{min}	μ_{max}
Amalthea (A34)	2.4	38	26	1.2	4.1×10^{15}	26.4	0.35	1.04
Io (I0)	5.8	26	28	2.0	1.3×10^{18}	17.3	0.16	1.17
Europa (E12)	8.7	21	30	2.0	2.7×10^{16}	13.7	0.03	1.28
Ganymede (G7)	12.0	18	40	1.7	2.8×10^{16}	10.9	0.12	1.33
Callisto (C3)	20.8	15	51	1.4	2.1×10^{15}	8.2	0.32	1.42
Enceladus (Enc 1)	3.4	20	30	2.0	3.6×10^{14}	12.6	0.15	1.11
Dione	5.7	17	31	2.0	2.1×10^{15}	10.0	0.02	1.16
Rhea (targeted)	7.8	15	31	2.0	1.3×10^{15}	8.5	0.08	1.21
Hyperion	22.5	12	55	1.4	5.2×10^{11}	5.1	0.38	1.22
Iapetus	50.4	11	57	1.4	5.0×10^{11}	3.3	0.58	1.17
Phoebe	156	10	50	1.2	6.8×10^{10}	1.7	0.79	1.13

values of μ, which correspond to conjunction and opposition, respectively. We can see that a substantial anisotropy is expected for all listed moons.

3. Dust distribution around a parent body

3.1. General problem

In general, we formulate the problem in the following way. Consider a dust parent body (planet or planetary satellite) without an atmosphere. Hypervelocity impacts of micrometeoroids, interstellar grains or ring particles onto the surface of the body eject dust grains that form a dust cloud around it. The dust production from the surface is modelled with a DF

$$f = f(\vec{r}_M, \vec{u}), \tag{19}$$

where $\vec{r}_M$ and $\vec{u}$ are the radius vector of a point on the surface and the initial velocity of the grain, respectively. Then, the number of grains ejected from the area $[\vec{r}_M, \vec{r}_M + d\vec{r}_M]$ of the surface with velocities $[\vec{u}, \vec{u} + d\vec{u}]$ is proportional to $f\, d^2\vec{r}_M\, d^3\vec{u}$. Note that a DF may generally involve other variables, such as the time or the grain mass. These additional dependencies are not considered here.

The dust cloud formed around the parent body is most generally described with the one-particle phase-space DF, provided that mutual interactions between the dust particles are negligible:

$$n = n(\vec{r}, \vec{v}), \tag{20}$$

where $n\, d^3\vec{r}\, d^3\vec{v}$ is the number of dust grains in the cloud located in volume $[\vec{r}, \vec{r} + d\vec{r}]$ with the velocities $[\vec{v}, \vec{v} + d\vec{v}]$. The arguments of n are the phase-space coordinates apart from the moon surface.

The problem we address here is to find the DF $n(\vec{r}, \vec{v})$ for a given initial ejecta DF $f(\vec{r}_M, \vec{u})$, under the assumption that the dynamics of the ejecta are known. In general the problem is intricate, since the dust dynamics cannot be described

analytically in most cases. Furthermore, the initial DF f is poorly known, as the surface of the moon and impact ejection process can be very complex. However, a formal general solution can be written:

$$n(\vec{r}, \vec{v}) = \left| \frac{\partial(\vec{r}_M, \vec{u})}{\partial(\vec{r}, \vec{v})} \right| n(\vec{r}_M, \vec{u}). \tag{21}$$

The initial (at the surface) and final (in the cloud) DFs, $n(\vec{r}_M, \vec{u})$ and $n(\vec{r}, \vec{v})$, are connected via the Jacobian of the transformation of variables, which is wholly determined by the particle dynamics. Since collisions and mutual interactions between the particles are disregarded, the phase-space DF and one-particle DF are one and the same. The phase-space DF at the surface is then given by

$$n(\vec{r}_M, \vec{u}) = \text{geom.factor} \times \text{total.rate}$$
$$\times f(\vec{r}_M, \vec{u})/\text{velocity}. \tag{22}$$

The term "geom.factor" arises from the coordinate system used, "total.rate" is the total number of particles ejected from the whole surface per unit time $[N^+B(\mu)$ in our model]. The factor "1/velocity" compensates the elapsed time (from N^+dt) and the coordinate normal to the surface (f is defined at the surface).

The approach used here originates from statistical physics. We consider a particular case when the particles do not interact with each other. Provided that no dissipative effects influence the dynamics, the phase-space volume is conserved. This is equivalent to the fact that $n(\vec{r}, \vec{v})$ has to satisfy the Liouville theorem:

$$\frac{Dn}{Dt} \equiv \frac{\partial n}{\partial t} + \vec{v} \cdot \frac{\partial n}{\partial \vec{r}} - \frac{\partial \Phi}{\partial \vec{r}} \cdot \frac{\partial n}{\partial \vec{v}} = 0, \tag{23}$$

where Φ denotes the potential of conservative external forces. It would be more correct to say that $n(\vec{r}, \vec{v})$ satisfies the collisionless Boltzmann equation (Vlasov equation), but without mutual particle interactions it is the same equation, i.e. the N-body DF is product of the one-particle DFs. The calculations made here are rather lengthy, and at the
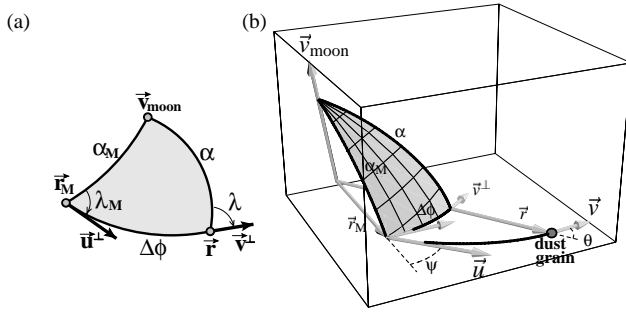
(a)   (b)

Fig. 4. The trajectory of the dust grain ejected from the surface of the satellite (shaded area). (a) Trajectory on the unit sphere and spherical geometry of angles: $\Delta\phi$, α, α_M, λ, λ_M. The vectors $\vec{r}$, $\vec{r}_M$, and $\vec{v}_{moon}$ are projected onto the unit sphere, becoming points on the surface of the sphere, while tangential components of velocities $\vec{v}^\perp$ and $\vec{u}^\perp$ determine velocity clock angles λ and λ_M: $\lambda = \measuredangle(\vec{v}_{moon}^\perp, \vec{v}^\perp)$, $\vec{v}^\perp \cdot \vec{r} = \vec{v}_{moon}^\perp \cdot \vec{r} = 0$. The sides of the spherical triangle are α, α_M and $\Delta\phi$, for $\Delta\phi < \pi$. if $\Delta\phi > \pi$, then the triangle is formed out of α, α_M and $2\pi - \Delta\phi$. (b) The trajectory in space for the particular choice: $\tilde{r} = 1.8$, $\alpha = 1.4$, $\tilde{v} = 0.35$, $\theta = 1$, $\lambda = 2$. The figure is oriented in such a way that the trajectory lies in the bottom box plane.

end we use Eq. (23) to ultimately test the outcome of our calculations—the phase-space DF $n(\vec{r}, \vec{v})$.

In the rest of this section, we elaborate Eqs. (21) and (22), considering only the gravity of the satellite. First, we write down these formulae in the above-introduced spherical coordinates (Section 3.2). Then we use integrals of the motion, those of the mechanical energy and momenta together with the spherical trigonometry to derive transformation formulae and the Jacobian (Section 3.3). In this way, we avoid explicit use of the time variable and the Kepler equation.

3.2. Calculation of the phase-space distribution function

Consider two phase-space points $(\vec{r}, \vec{v})$ and $(\vec{r}_M, \vec{u})$ which correspond to a position above the surface and to a launch point at the surface of the satellite, respectively. We use spherical coordinate systems in the configuration space, $\vec{r}_M(r_M, \alpha_M, \beta_M)$ and $\vec{r}(r, \alpha, \beta)$, and in the velocity space, $\vec{u}(u, \psi, \lambda_M)$ and $\vec{v}(v, \theta, \lambda)$. The Z_v-axes of the velocities are the radius vectors of the related point in space [see Figs. 1 and 4 and Eq. (10)]. Note that both f and n are independent of the longitudes β_M and β, respectively, and in what follows they will be dropped from expressions.

We start with the initial ejecta DF which is given in its general form by

$$f = f(\alpha_M, u, \psi, \lambda_M). \tag{24}$$

The ranges of the angles are: $\psi \in [0, \pi/2]$, $\theta \in [0, \pi]$, $\alpha, \alpha_M \in [0, \pi]$, and $\lambda, \lambda_M \in [0, \pi]$. Given the initial DF (24), the resulting phase-space DF is generally written as $n = n(r, \alpha, v, \theta, \lambda)$, defining the number of particles in the infinitesimally small volume of the phase-space around a

point $(\vec{r}, \vec{v})$

$$dn = n(r, \alpha, v, \theta, \lambda) 2\pi \sin\alpha\, r^2\, dr\, d\alpha \sin\theta\, v^2\, dv\, d\theta\, d\lambda, \tag{25}$$

where the factor 2π results from integration over β. The point $(\vec{r}, \vec{v})$ defines the trajectory of the dust particle, determined by the initial condition $(\vec{r}_M, \vec{u})$. Thus, the number dn of particles ejected from the initial point [Eq. (9)], later contribute to the phase-space DF in orbit. Provided that dn is constant, the question is which volume they occupy later while in orbit. In other words, the dynamics, defining the change of the shape of the phase-space volume element, is the link between the initial DF f and the final one n. This is only valid because the dust particles do *not* interact with each other. Consequently, equating expressions (25) and (9) we arrive at the phase-space DF:

$$n(r, \alpha, v, \theta, \lambda) = \frac{N^+ B(\mu)}{2\pi r^2 v^2 \sin\alpha \sin\theta} f(\alpha_M, u, \psi, \lambda_M)$$

$$\times \frac{1}{|\dot{r}|} \left| \frac{\partial(\alpha_M, u, \psi, \lambda_M)}{\partial(\alpha, v, \theta, \lambda)} \right|. \tag{26}$$

The expression is a specific version of formulae (21) and (22) in the coordinate system used here. We have to find initial coordinates as a function of those ones along the orbit, and to calculate the Jacobian of this transformation $(\alpha_M, u, \psi, \lambda_M) \xrightarrow{r} (\alpha, v, \theta, \lambda)$. The radius r is considered as the parameter of the transformation.

The number of arguments in the initial and the final DFs, f and n, is different. The initial function f depends on four coordinates $(\alpha_M, u, \psi, \lambda_M)$ whereas the final DF depends on five coordinates $(r, \alpha, v, \theta, \lambda)$. However, the Jacobian is unambiguously defined. The dynamics (in this case two-body problem) defines the family of trajectories in the phase-space, which do not intersect each other. If the phase-space is N-dimensional, there is one independent variable along the trajectory, while other $N - 1$ coordinates are dependent and $N - 1$ is the dimension of a set of the initial coordinates as well. The dependent coordinates contribute to the Jacobian, while the Nth coordinate (here r) interval determines the time interval needed to calculate the number of ejected particles ($N^+ dt$).

3.3. Dust particle dynamics

In this section we calculate the dependence of the phase-space coordinates of the orbital motion on the initial ones as well as the Jacobian, The calculations are done in much the same way as in PAPER I, and we describe them only briefly.

The dynamics are simply given by the two-body problem, formulated here in dimensionless quantities. First, we assume the unit mass of a dust grain. Then, we scale radial coordinates with the radius of the moon r_M and the velocities with the surface escape velocity $v_{esc} = \sqrt{2GM_{moon}/r_M}$:

$\tilde{r} = r/r_M$, $\tilde{u} = u/v_{esc}$, and $\tilde{v} = v/v_{esc}$. From integrals of the motion, those of mechanical energy and angular momenta,

$$\frac{2E_K}{v_{esc}^2} \equiv \tilde{u}^2 - 1 = \tilde{v}^2 - \frac{1}{\tilde{r}},$$

$$\frac{L}{v_{esc} r_M} \equiv \tilde{u} \sin \psi = \tilde{r} \tilde{v} \sin \theta, \qquad (27)$$

we get the transformation rules

$$\tilde{u}(\tilde{v}) = \sqrt{\tilde{v}^2 + 1 - 1/\tilde{r}}, \quad \psi = \psi(\tilde{v}, \theta). \qquad (28)$$

Next, a parameterization of an orbit in the plane of the motion is introduced by

$$\tilde{r} = \frac{\tilde{p}}{1 + e \cos \phi}, \qquad (29)$$

where ϕ, e, $p = a(1 - e^2)$, a are the true anomaly, eccentricity, latus rectum and semimajor axis of the orbit. Using the conserved values, the mechanical energy E_K and angular momentum L, yields

$$\tilde{p} \equiv \frac{L^2}{GMr_M} = 2\tilde{r}^2 \tilde{v}^2 \sin^2 \theta, \qquad (30)$$

$$e^2 \equiv 1 + \frac{2E_K L^2}{G^2 M^2} = 1 + 4\tilde{r}^2 \tilde{v}^2 \sin^2 \theta \left(\tilde{v}^2 - \frac{1}{\tilde{r}} \right). \qquad (31)$$

The true anomalies of the launch point ϕ_M, and during the orbital motion ϕ, are given by

$$\cos \phi_M = \frac{1}{e} \left[\frac{\tilde{p}}{1} - 1 \right], \quad \cos \phi = \frac{1}{e} \left[\frac{\tilde{p}}{\tilde{r}} - 1 \right]. \qquad (32)$$

Then, the separation angle $\Delta \phi \equiv \phi - \phi_M$ is the angle flanked by radius vectors at ejection $\vec{r}_M$ and along the trajectory $\vec{r}$ (see Fig. 4). It depends on $\tilde{v}$ and θ only (radius $\tilde{r}$ is always considered as a parameter).

In order to calculate the angles α_M and λ_M as functions of final coordinates, we project the trajectory of the dust grain and all vectors onto the unit sphere (Fig. 4). Here we implicitly use the integrals of the motion: the trajectory is located in the plane, and angles α and λ can be obtained by considering the geometry alone. The projected trajectory and spherical lines between the velocity of the moon and radius vectors $\vec{r}_M$ and $\vec{r}$ form a spherical triangle. The plane of the motion is constant and contains the radius and velocity vectors. Its intersection with the unit sphere defines the projected trajectory— a line on the unit sphere. Then, the angles α, α_M and $\Delta \phi < \pi$ are sides of the spherical triangle, while $\pi - \lambda$ and λ_M are angles of the spherical triangle encompassing the side $\Delta \phi$ (Fig. 4a). Using spherical trigonometry we obtain the following relations:

$$\frac{\sin \alpha}{\sin \lambda_M} = \frac{\sin \alpha_M}{\sin(\pi - \lambda)}, \qquad (33)$$

$$\cos \alpha_M = \cos \alpha \cos \Delta \phi + \sin \alpha \sin \Delta \phi \cos(\pi - \lambda), \qquad (34)$$

$$\cos \alpha = \cos \alpha_M \cos \Delta \phi + \sin \alpha_M \sin \Delta \phi \cos \lambda_M. \qquad (35)$$

Eq. (33) is the consequence of the law of sines, and Eqs. (34) and (35) are based on the law of cosines. Expression (34) immediately gives the transformation rule for α_M. Replacing $\sin \alpha_M$ and $\cos \alpha_M$ in Eq. (35) we get:

$$\cot \lambda_M = \cot \alpha \frac{\sin \Delta \phi}{\sin \lambda} + \cot \lambda \cos \Delta \phi. \qquad (36)$$

Another possibility is that $\Delta \phi > \pi$, when the spherical triangle is formed with sides α, α_M and $2\pi - \Delta \phi$ and angles $\pi - \lambda_M$ and λ, but relations (33)–(36) hold in this case as well.

After lengthy, but straightforward, differentiation and algebraic manipulation, using Eqs. (27), (34) and (36), we arrive at the expression for the Jacobian:

$$\left| \frac{\partial(\alpha_M, \tilde{u}, \psi, \lambda_M)}{\partial(\alpha, \tilde{v}, \theta, \lambda)} \right|_{\tilde{r}} = \frac{\tilde{r} \tilde{v}^2}{\tilde{u}^2} \frac{|\cos \theta|}{\cos \psi} \frac{\sin \alpha}{\sin \alpha_M}. \qquad (37)$$

Here the radius $\tilde{r}$ is taken as a constant parameter for evaluation of the corresponding partial derivatives. The remaining term $\dot{r}$ is simply $\dot{r} = v \cos \theta$. Inserting this into Eq. (26) we obtain the final expression for the phase-space DF:

$$n(\tilde{r}, \alpha, \tilde{v}, \theta, \lambda) = \frac{N^+ B(\mu)}{2\pi r_M^2 v_{esc}^3} \frac{1}{\tilde{r} \tilde{v} \tilde{u}^2} \frac{1}{\sin \theta \cos \psi \sin \alpha_M}$$
$$\times f(\alpha_M, \tilde{u}, \psi, \lambda_M), \qquad (38)$$

where initial variables α_M, $\tilde{u}$, ψ, and λ_M are substituted from Eqs. (34), (28), and (36). In the next section, we discuss the domain where the DF (38) is defined: the one where $n > 0$.

Expression (38)—multiplied by 2π—still stands even in the most general case (not discussed here), when f is dependent on the longitude β_M. This is simply because β_M is the rotational angle around axis $\vec{v}_{moon}$ and the Jacobian remains the same. Then, the phase-space DF n depends on all phase-space coordinates, including the longitude β, and the additional transformation

$$\beta_M(\tilde{r}, \alpha, \beta, \tilde{v}, \theta, \lambda) = \beta \pm \arcsin[\sin \Delta \phi \sin \lambda / \sin \alpha_M] \qquad (39)$$

can be obtained from spherical trigonometry as well.

4. Number density

In this section we combine the results from the Sections 2 and 3. Once the general phase-space DF, Eq. (38), has been obtained, all quantities of interest can be calculated as moments of the DF. A quantity of greatest practical utility is the number density of dust, which is the zeroth moment of DF:

$$n(\tilde{r}, \alpha) = \int d^3 \tilde{v} \, n(\tilde{r}, \alpha, \tilde{v}, \theta, \lambda). \qquad (40)$$

The integration has to be carried out over a domain of velocities where the general DF is properly defined. The integration domain is elaborated in turn for bound grains, those in elliptic Keplerian orbits, and for unbound or escaping

dust grains in hyperbolic orbits. Then, as a reference case, we consider the spherically symmetric dust production, and finally we study asymmetry effects.

4.1. Orbit types for dust grains

In the case of *bound* (elliptic) orbits the mechanical energy is negative and the velocities at a certain distance $\tilde{r}$ must satisfy

$$\tilde{v} < \tilde{v}_C(\tilde{r}) = \tilde{r}^{-1/2}. \tag{41}$$

Here $\tilde{v}_C(\tilde{r})$ is the scaled escape velocity at the distance $\tilde{r}$. The conservation of the angular momenta provides the domain for the angle θ (for details see PAPER I, Fig. 4 ibid):

$$\theta \in [0, \theta_C] \cup [\pi - \theta_C, \pi], \tag{42}$$

where

$$\theta_C(\tilde{r}, \tilde{v}) = \begin{cases} \pi/2, & 0 \leqslant \tilde{v} \leqslant \tilde{v}_1, \\ \arcsin[\tilde{u}(\tilde{r}, \tilde{v})/(\tilde{r}\tilde{v})], & \tilde{v}_1 < \tilde{v}, \end{cases} \tag{43}$$

and $\tilde{v}_1 = l/\sqrt{\tilde{r}(\tilde{r}+1)}$. The latter is the maximum velocity a particle can have at $\tilde{r}$, so that the complete elliptical orbit touches the satellite surface at the pericenter. Any higher velocity would result in a higher energy, meaning an increase of the semimajor axis with the consequence that the orbit no more intersects the surface of the moon for all $\theta \in [0, \pi]$. The intersection of all orbits (also the unbound ones) with that surface is a necessary requirement because all matter originates from there, i.e. all orbits have to meet the surface–bound ones in 2 points, the unbound hyperbolic ones only at the launch point. These requirements are equivalent to the existence of a solution for u and ψ. The first branch $\theta < \theta_C$ of Eq. (42) corresponds to bound particles which depart from the moon, and $\theta > \pi - \theta_C$ to returning particles. Since the shape of the trajectory is completely determined by the set $(\tilde{r}, \tilde{v}, \theta)$, conditions (41) and (42) ensure that the trajectory intersects the surface of the moon. The remaining arguments, angles α and λ, just determine the orientation of the orbit in the space. Therefore, the number density for bound grains is given by

$$n_{\text{bound}}(\tilde{r}, \alpha)$$

$$= v_{\text{esc}}^3 \int_0^{\tilde{v}_C} \int_0^{\theta_C} \int_0^{\pi} \tilde{v}^2 \, d\tilde{v} \sin\theta \, d\theta \, d\lambda \, n(\tilde{r}, \alpha, \tilde{v}, \theta, \lambda)$$

$$+ v_{\text{esc}}^3 \int_0^{\tilde{v}_C} \int_{\pi-\theta_C}^{\pi} \int_0^{\pi} (\ldots) \tag{44}$$

The factor v_{esc}^3 is the consequence of the scaling of velocities and the argument of the second integral is the same as the argument of the first integral.

For *escaping* (unbound, hyperbolic) grains, the mechanical energy is positive, and we get: $\tilde{v} > \tilde{v}_C(\tilde{r})$. Since the particle cannot return from the infinity, we have $\theta < \pi/2$: $\theta \in [0, \theta_C]$. Then, the resulting number density for the

unbound particles is

$$n_{\text{unbound}}(\tilde{r}, \alpha) = v_{\text{esc}}^3 \int_{\tilde{v}_C}^{\infty} \int_0^{\theta_C} \int_0^{\pi} \tilde{v}^2 \, d\tilde{v} \sin\theta \, d\theta \, d\lambda$$

$$\times n(\tilde{r}, \alpha, \tilde{v}, \theta, \lambda). \tag{45}$$

4.2. Spherically symmetric case

Let us re-examine the model of the spherically symmetric dust production (PAPER I):

$$f^{(\text{symm})}(\alpha_M, \tilde{u}, \psi, \lambda_M) = f_{u,\psi}(\tilde{u}, \psi) \frac{\sin\alpha_M}{2\pi}, \tag{46}$$

where the geometrical factor $\sin\alpha_M/(2\pi)$ is a consequence of normalization (11). The number of ejecta does not depend on the location on the surface of the moon α_M. We have:

$$n^{(\text{symm})}(\tilde{r}) = \frac{N^+ B(\mu)}{4\pi r_M^2} \frac{1}{\tilde{r}} \int_{\tilde{v}} \int_{\theta} d\tilde{v} \, d\theta \, \frac{\tilde{v}}{\tilde{u}^2 \cos\psi}$$

$$\times f_{u,\psi}(\tilde{u}, \psi), \tag{47}$$

where $\int_{\tilde{v}} \int_{\theta}$ denote the integration domains, as defined in Eqs. (44) and (45). In the spherically symmetric case, $\mu = 0$ and $B(0) = 1$. Eq. (47) coincides with the expression for the number density derived in PAPER I.

4.3. Asymmetric case

In order to study the asymmetric case we use the analytical ansatz of the initial DF of ejecta $f_\alpha(\alpha_M)$ proposed in Section 2.2, Eq. (14):

$$f(\alpha_M, \tilde{u}, \psi, \lambda_M)$$

$$= f_{u,\psi}(\tilde{u}, \psi) \frac{\sin\alpha_M}{2\pi} \left(1 + C^{(1)} \mathbf{P}_1(\alpha_M) + \cdots\right), \tag{48}$$

where Legendre polynomials are $\mathbf{P}_1(\alpha_M) = \cos\alpha_M$, and so on. Although this initial DF f is independent of the clock angle λ_M, the resulting final DF n depends on λ via $\alpha_M = \alpha_M(\tilde{r}, \alpha, \tilde{v}, \theta, \lambda)$, Eq. (34). This is simply a consequence of the geometry of the problem. However, in order to obtain the number density we can integrate over λ (Appendix B), and the result is

$$n(\tilde{r}, \alpha) = n^{(\text{symm})}(\tilde{r})$$

$$\times [1 + C^{(1)}(\mu) \times c_1(\tilde{r}) \times \mathbf{P}_1(\alpha) + \cdots]. \tag{49}$$

The quantity $n^{(\text{symm})}(\tilde{r}) = \int_0^{\pi} n(\tilde{r}, \alpha) \sin\alpha \, d\alpha/2$ is the number density in the spherically symmetric case, Eq. (47). Here, it is the averaged number density in the shell $[\tilde{r}, \tilde{r} + d\tilde{r}]$, with a geometrical weight $\sin\alpha/2$. The quantities $c_i(\tilde{r})$ are defined as

$$n^{(\text{symm})}(\tilde{r}) c_i(\tilde{r}) = \frac{N^+ B(\mu)}{4\pi r_M^2} \frac{1}{\tilde{r}} \int_{\tilde{v}} \int_{\theta} d\tilde{v} \, d\theta \, \frac{\tilde{v}}{\tilde{u}^2 \cos\psi}$$

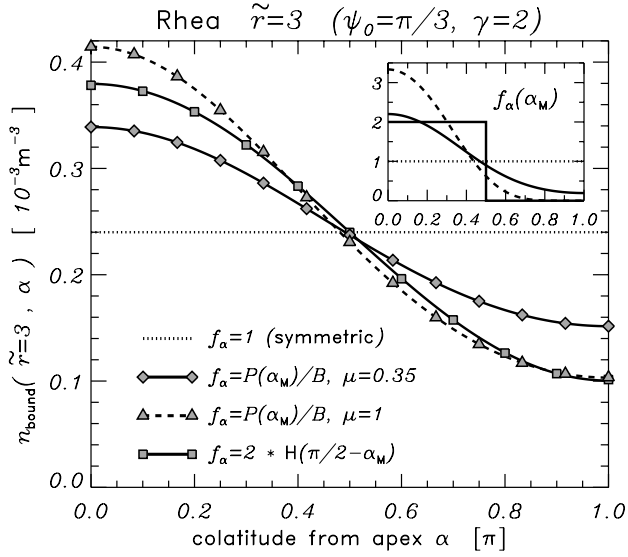$$\times f_{u,\psi}(\tilde{u}, \psi) \mathbf{P}_i(\Delta\phi), \tag{50}$$

Fig. 5. The number density of bound particles against the colatitude α for a fixed radius $\tilde{r} = 3$. The lines are result of Eq. (49) using the first three modes ($C^{(3)} = 0$), while symbols denote triple numerical integration of Eq. (44). The inset shows corresponding initial distributions of ejected dust grains from the surface versus the colatitude α_M (in π). The parameters are: $\psi_0 = \pi/3$, $\lambda = 2$. See text for details.

Fig. 6. The number density of bound particles as a function of the colatitude α for different radii $\tilde{r}$. The initial ejecta distribution is taken for $\mu = 1$. The profiles correspond to the dashed line in Fig 5, and the parameters are the same. The plotted symbols (triple numerical integration) are in excellent agreement with the analytical formula (line).

and they cover the range $c_i \in [-1, 1]$ and $c_i(1) = 1$ (by the definition from properties of Legendre polynomials). We stress again that the above results do not assume any particular choice of $f_{u,\psi}(u, \psi)$, while any given $f_\alpha(\alpha_M)$ can be incorporated through corresponding Legendre coefficients $C^{(i)}$.

In Fig. 5, the number density (49) is plotted as a function of the colatitude α, where $n^{(symm)}$ and c have been calculated numerically from Eqs. (47) and (50), in the case of the satellite Rhea (lines). Different lines stand for different initial distributions $f_\alpha(\alpha_M)$, and we used $B = 1$ in Eq. (47) to force the same absolute level [$B(\mu)$ is in the order of unity anyway]. Symbols in Fig. 5 represent the full numerical integration result of (44) for the corresponding production rate $P(\alpha_M)$ (lines in the inset). The agreement is excellent, and even taking just the first mode $\mathbf{P}_1(\alpha) = \cos \alpha$ would give fairly good results.

Fig. 6 shows the azimuthal part of the number density $n(\tilde{r}, \alpha)/n^{(symm)}(\tilde{r})$ for different radii $\tilde{r}$. We have taken the case of the moon Rhea for $\mu = 1$ when the asymmetry is quite pronounced. The number density quickly transforms into the cosine function as the distance $\tilde{r}$ increases. At the same time the amplitude of the asymmetry [basically given by $c_1(\tilde{r})$] decreases. For smaller μ, all the lines squeeze vertically with higher modes being even smaller. When $\mu = 0$, they all collapse to a horizontal line $n/n^{(symm)} = 1$.

Thus, in our cases only zeroth and first-order modes influence the results essentially inside the Hill sphere of the satellite, i.e. in the region where the gravity of the parent moon dominates the particle dynamics.
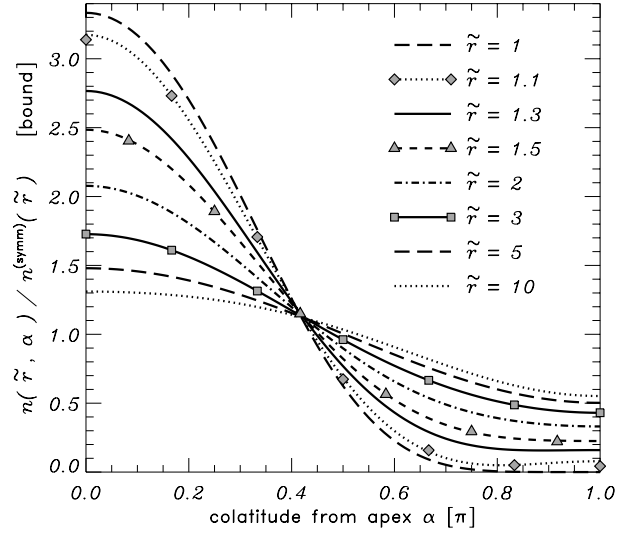
4.4. Variations of the initial DF

In this section, we examine the influence of the distribution of the initial velocities on the number density. For this purpose, we again factorize the initial DF $f_{u,\psi}(\tilde{u}, \psi) = f_u(\tilde{u}) f_\psi(\psi)$. We concentrate on two quantities: the average value $n^{(symm)}(\tilde{r})$ and the coefficient of asymmetry $c_1(\tilde{r})$. Fig. 7 shows both as functions of $\tilde{r}$ for different initial angular distributions of ejecta. As was shown in PAPER I, the average (spherically symmetric) number density depends largely on the speed distribution; only in the close vicinity of the moon ($\tilde{r} < 1.5$) does the angular distribution slightly affect the average density, as well.

In contrast to the average number density, the modulation factor $c_1(\tilde{r})$ depends strongly on the angular distribution (left panels in Fig. 7). The coefficient c_{bound} is always smaller than the $c_{unbound}$ indicating a weaker asymmetry contribution of the bound particles. This is because bound particles contribute twice, and the returning grains mostly originate at the opposite location compared to the location of the final point. Thus, in this case the "mixing" is stronger and the asymmetry decays more quickly with $\tilde{r}$. The total c is in between, and it is always larger than 0. At smaller distances, c_{total} is dominated by bound particles; at distances $\tilde{r} > 10$, the hyperbolic ones prevail.

Next, we consider a fixed speed distribution $f_u(\tilde{u})$ and examine the influence of $f_\psi(\psi)$. Panels (a)–(f) in Fig. 7 are drawn for the uniform distribution in the cone $\psi < \psi_0$, Eq. (18). If the opening angle ψ_0 is small (panel (a)) dust grains are ejected almost in the normal direction from the surface, and initial asymmetry persists away from the moon. For larger opening angles ψ_0 "mixing" of the
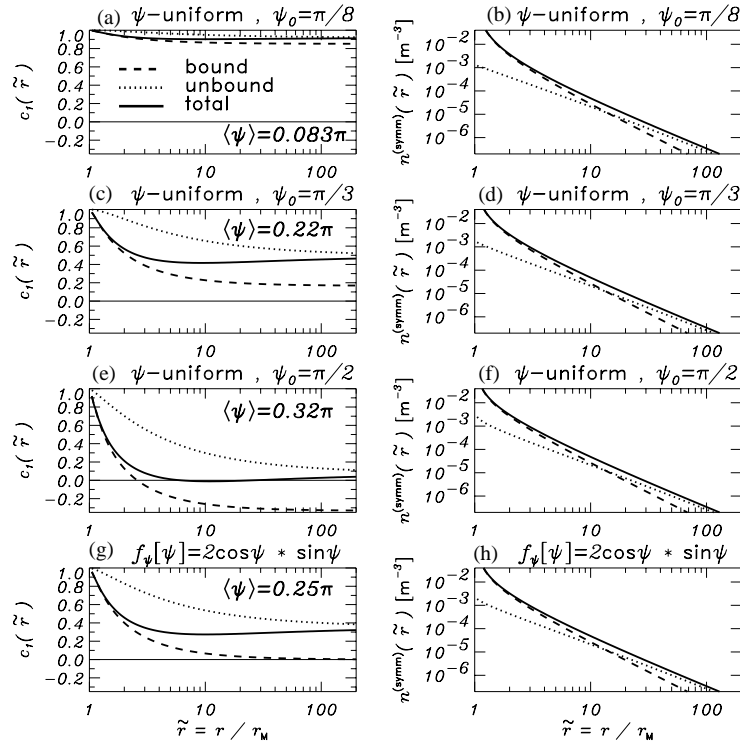
Fig. 7. The modulation factor $c_1(\tilde{r})$ (left panels) and the averaged number density $n^{(symm)}(\tilde{r})$ (right panels) for different initial distributions. The initial speed distribution is a power law (17), and panels (a)–(f) stand for uniform distribution in the cone $\psi < \psi_0$ for different ψ_0, while panels (g) and (h) represent $f_\psi(\psi) = 2\cos\psi \times \sin\psi$. The dashed line represents the bound particle contribution, the dotted line stands for the unbound (hyperbolic) contribution, and the solid line for the total. Note that the number densities differ only for radii close to the surface. Numerical values are assumed for Rhea and $\mu = 1$.

different parts of ejecta position is stronger and the asymmetry drops very quickly from the initial value of 1 (Fig. 7, panels c and e).

In the limiting case of a uniform distribution in the whole hemisphere $\psi = \pi/2$ (panel e), the bound part of the asymmetry coefficient c_1 becomes negative at $\tilde{r} > 3$. In Fig. 8, a comparison between two different uniform distributions $f_\psi \propto \sin\psi$ (panels a and b) and cosine modulated $f_\psi \propto \sin\psi \cos\psi$ (panel c) is made. An adjective "uniform" means that the probability is distributed uniformly with respect to the *solid angle*, causing the weighting term $\sin\psi$ in the distribution. The shaded areas in Fig. 8 represent equally probable intervals for ψ. It is apparent that in the case of the uniform distribution the particles are preferably ejected at large angles ψ, because the corresponding solid angle $d\Omega = 2\pi \sin\psi \, d\psi$ is then larger. Additionally, the majority of particles are launched from the leading hemisphere owing to the asymmetry f_α. Furthermore, the separation between the initial and final point $\Delta\phi$ of particles with $\psi \approx \pi/2$ is quite close to π, which means that the probability of finding of such bound particles is higher at locations opposite from their location at launch. Together with the asymmetry effect, this leads to the unusual situation that more bound particles (those with $\psi \approx \pi/2$) populate the trailing hemisphere than the leading one. However, this is just a consequence of an unrealistic choice of the initial distribution $f_\psi(\psi)$.

In order to examine the dependence of $c(\tilde{r})$ on the initial directional distribution $f_\psi(\psi)$ in more detail, we have calculated the number densities for two additional ψ distributions. The first one is in the form of the cosine modulation of the uniform distribution:

$$f_\psi(\psi) = \frac{2\cos\psi}{\sin^2\psi_0} \sin\psi \, H[\psi_0 - \psi], \tag{51}$$

where ψ_0 is again the opening angle. For $\psi_0 = \pi/2$ the number of particles having small and large ψ are balanced (panel c in Fig. 8). The cosine term simply reduces the number of particles with angles ψ close to $\pi/2$. The resulting asymmetry coefficient c and the averaged number density n are shown in Fig. 7 (panels g and h). As expected, the density $n^{(symm)}(\tilde{r})$ is the same as in the uniform ejecta case, but c_{bound} becomes positive for all $\tilde{r}$ now. More precisely, the asymmetry coefficients are similar to the case of $\psi_0 = \pi/3$ of the uniform distribution. As with the average number density $n^{(symm)}$, also asymmetry coefficients c are not very sensitive to an exact form of $f_\psi(\psi)$. We find that only the mean initial angle ψ is of importance:

$$\langle\psi\rangle = \int_0^{\pi/2} \psi f_\psi(\psi) \, d\psi \tag{52}$$

To check this, we have studied the "degenerate" case, when we allow only $\psi = \langle\psi\rangle$, or $f_\psi(\psi) = \delta(\psi - \langle\psi\rangle)$,
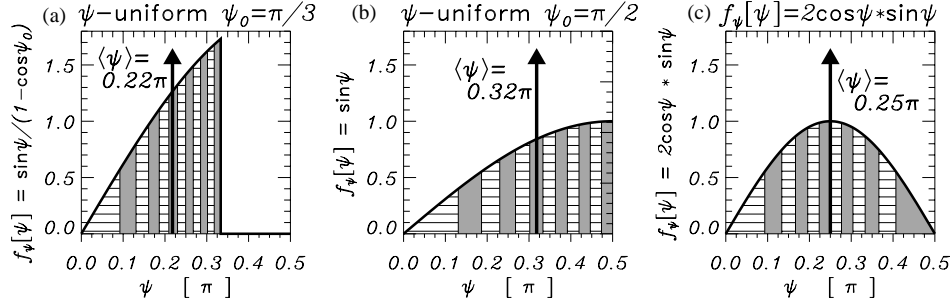
Fig. 8. Comparison between different initial distribution functions of the angle ψ. The shaded areas are ψ intervals of the equal probability 1/12. The arrows represent the equivalent Dirac delta distributions. Their abscissae correspond to the mean angle $\langle\psi\rangle$.
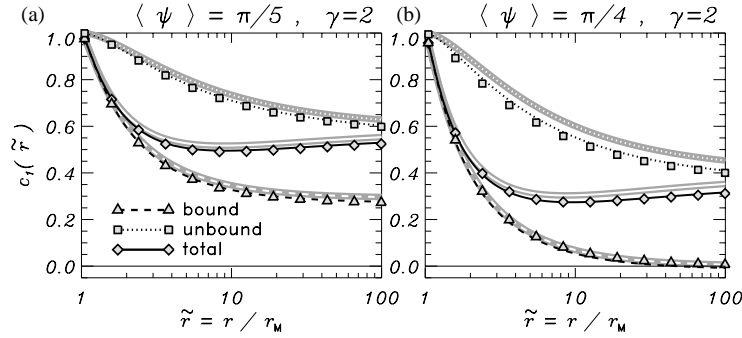

Fig. 9. Asymmetry coefficients $c_1(\tilde{r})$ calculated for different initial distributions $f_\psi(\psi)$, with fixed mean angle $\langle\psi\rangle = \pi/5$ (a) and $\langle\psi\rangle = \pi/4$ (b). Lines stand for the uniform distribution in a cone ψ_0, symbols for the distribution (51) in a cone ψ_0, and thick gray lines for the Dirac delta distribution $f_\psi(\psi) = \delta(\psi - \langle\psi\rangle)$. The opening angles ψ_0 depend on the type of the distribution and mean value $\langle\psi\rangle$. The overall agreement is excellent.

and compared the results with those for the complete distributions (uniform, cosine-modulated). A comparison presented in Fig. 9 makes it evident that indeed, the asymmetry coefficients c depend only on the mean angle $\langle\psi\rangle$ of the ejecta.

Replacing the initial angular distribution with delta-distribution reduces Eq. (50) to a single integral and so simplifies the calculation of coefficients c considerably. Using the methods outlined in PAPER I we find

$$c_{1,\text{bound}}(\tilde{r}) = \cos(2\langle\psi\rangle) + 2\sin^2\langle\psi\rangle \frac{2+\cos(2\langle\psi\rangle)}{3}\frac{1}{\tilde{r}}$$
$$+ \mathrm{O}[\tilde{r}^{-2}]. \tag{53}$$

The expansion works well already for $\tilde{r} > 2.5$. The dust particles in the hyperbolic orbits obey

$$\lim_{\tilde{r}\to\infty} c_{1,\text{unbound}}(\tilde{r}) \approx \cos(3\langle\psi\rangle/2), \tag{54}$$

while the next term behaves as $\mathrm{O}[\tilde{r}^{-1/2}]$. The coefficients $c_2(\tilde{r})$ for the second-order correction can be approximated as: $c_{2,\text{bound}}(\tilde{r}) \approx \tilde{r}^{-2}$ and $c_{2,\text{unbound}}(\tilde{r}) \approx \tilde{r}^{-1}$.

The coefficients $c(\tilde{r})$ are nearly insensitive to the slope of the cumulative speed distribution γ. This can be seen from series (53) which contains no term with γ. The difference between curves with $\gamma = 1.2$ and 2 is even less than the

difference between $f_\psi(\psi)$ distribution curves in Fig. 9, and it vanishes at infinity.

To summarize, out of all the parameters of the initial speed and angular distributions of ejecta, the asymmetry coefficients $c(\tilde{r})$ largely depend only on a parameter, the mean ejection angle $\langle\psi\rangle$. It is interesting that the above-mentioned difference of $n^{(\text{symm})}$ curves close to the moon (Fig. 7) can also be attributed to $\langle\psi\rangle$ solely (for a fixed speed DF f_u).

4.5. Applications

The scaled satellite velocity $\mu = v_{\text{moon}}/v_{\text{IDPs}}$ determines the asymmetric production at the surface. The propagation of this initial asymmetry to larger distances (if any $\mu > 0$) solely depends on the mean ejecta angle $\langle\psi\rangle$. We therefore give a brief outline of experimental data on the angular distribution of ejecta.

Recent impact experiments into ice-silicate mixtures by Koschny and Grün (2001a,b) provide some information about directional distributions of the ejecta. They found that the measured data can be described by a Gaussian distribution

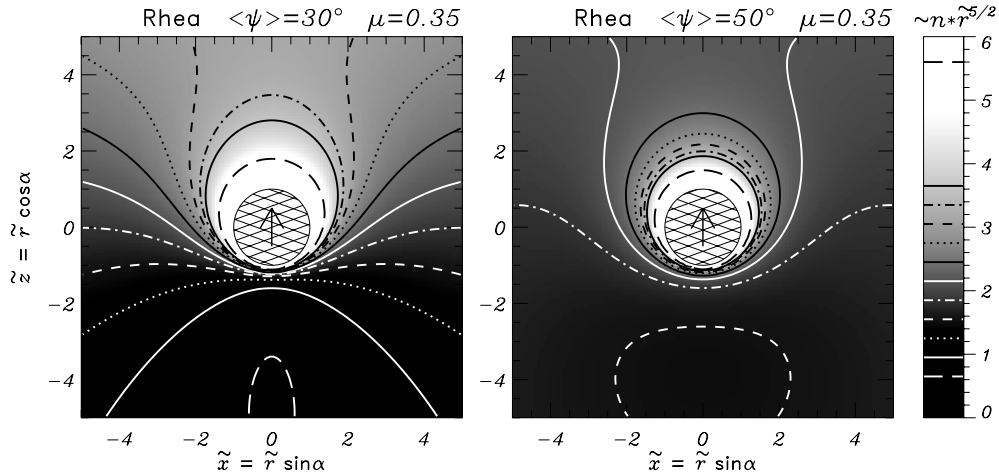$$f_\psi(\psi) = N \exp\left[-\frac{(\psi - \psi_{\text{max}})^2}{2w^2}\right], \tag{55}$$

Fig. 10. Color-scale plots of the number density (in the plane $y = 0$) with over-plotted isolines for two values of $\langle \psi \rangle$. The number density is multiplied with $\tilde{r}^{5/2}$ and a constant. The moon (hatched circle) moves in the direction of z-axis.

where $\psi_{max} = 20.5°$ and $w = 16°$ is the half-width of the distribution, while the constant N is chosen in such a way that $\int d\psi f_\psi(\psi) = 1$. We find again that the coefficients $c(\tilde{r})$ depend on the mean ejecta angle only, and the profiles fall on top of those in Fig. 9 and closer to a $\delta(\psi - \langle \psi \rangle)$ case since DF is more confined. Using the above experimental parameters we obtain $\langle \psi \rangle = 24°$. This value implies more pronounced asymmetry effects than those shown in Fig. 9a.

However, there are many experimental limitations, and the above values have to be taken with care. Other experiments with normal impacts (Hartmann, 1985; Frisch, 1992; Burchell et al., 1998) also suggest ejection of particles close to the normal of the surface—we estimate $\langle \psi \rangle$ as 30° or even less (Frisch, 1992). But, impacts of micrometeoroids onto atmosphereless bodies in the solar system are most probably oblique. Recent experiments with oblique impacts (Yamamoto and Nakamura, 1997; Yamamoto, 2002) imply a nontrivial (ψ, λ_M) ejecta distribution, dependent on the impactor incident angle. The overall $f_\psi(\psi)$ is less confined and the mean angle $\langle \psi \rangle$ is probably greater than 30°. Other effects reported to be typical of oblique impacts, such as ejecta "jetting" or "ricochet" (e.g., Weidenschilling and Davis, 1986), may introduce further complications.

In Fig. 10, we show the scaled number density in the equatorial plane ($y = 0$) of Rhea for two values of $\langle \psi \rangle$. The Z-axis is the direction of the satellite motion in the inertial frame of reference, and we have taken $\mu = 0.35$. This value lies well within the possible range for Rhea (Table 2) and the initial asymmetry is still very pronounced: $C^{(1)}(0.35) = 1$. We multiplied the number density by $\tilde{r}^{5/2}$, since $\tilde{r}^{-5/2}$ is the asymptotic behavior for the dust particles in bound orbits (PAPER I), which are dominant in the range $\tilde{r} < 5$. In this way, we removed most of the symmetric contribution $n^{(symm)}(\tilde{r})$, except in the very close proximity of the

moon $\tilde{r} < 1.5$. The values in Fig. 10 are dimensionless: the quantity $n(\tilde{r}, \alpha) \times \tilde{r}^{5/2}$ is scaled with the constant (see also PAPER I)

$$\frac{N^+ B(\mu)}{2\pi r_M^2 v_{esc}} \gamma \left(\frac{u_0}{v_{esc}} \right)^\gamma = 3.0 \times 10^{-3} \, \text{m}^{-3}. \quad (56)$$

The experimentally suggested value of the mean ejecta direction $\langle \psi \rangle = 30°$ leads to a pronounced asymmetry of the dust cloud, clearly seen in Fig. 10a. In contrast, the value $\langle \psi \rangle = 50°$ (Fig. 10b) gives a nearly symmetric dust distribution, except in the very close vicinity of the moon.

Although the above example is given for Rhea, the asymmetries of the dust clouds around other satellites are similar, only the absolute levels differ. The only satellite-specific parameters in the asymmetric part of the number density distribution are the ratio of the satellite instantaneous speed to the impactor speed (μ) and the mean ejecta angle ($\langle \psi \rangle$), the latter depending on the satellite surface properties. As noted in Section 2.3 and is clearly seen from Table 2, the maximum value of μ for satellites of Jupiter and Saturn is on the order of 1. Fig 3 suggests that $C^{(1)}$ is in order of 1 as well. Expression for the number density (49) shows, then, that the relative latitudinal variation of the cloud density at a given distance $\tilde{r}$ from the satellite center is closely approximated by the coefficient $c_1(\tilde{r})$. Calculating $c_1(\tilde{r})$ by using Eq. (53) or taking its values from figures (e.g. Fig. 7), we obtain an estimate of the cloud asymmetry for any satellite at any distance $\tilde{r}$.

5. Summary

This paper extends the model of an impact-generated, steady-state dust cloud around an atmosphereless planetary satellite or planet (Krivov et al., 2003) from spherically

symmetric to a more general asymmetric case. The asymmetry effects are assumed to result from the motion of the parent body through an isotropic field of impactors. As in the spherically symmetric case, we consider in turn the dust production from the surface, derive a general phase-space DF (distribution function) of dust, and then construct a model that can provide the expected density field and fluxes on the dust instruments onboard space missions like *Galileo* and *Cassini* in the vicinity of the parent body.

5.1. Dust production model

The asymmetric dust production is modelled by constructing an initial DF f, which depends on the colatitude α_M measured from the apex of the satellite motion. The latter provides the origin of this asymmetry, since impactors strike more frequently the leading hemisphere than the trailing one and their speeds are higher at the leading hemisphere. Comparing dynamical time scales, we conclude that the orbital period of the satellite is much longer than the average time an ejected dust particle spends in the cloud. Then, we simply assign an asymmetry coefficient $C^{(1)}(\mu)$ to the dust production model, which depends on the satellite position on the orbit, since the formation of clouds is an adiabatic process. The parameter $\mu = v_{\mathrm{moon}}/v_{\mathrm{IDPs}}$ measures the speed of the parent moon in the inertial frame of reference (with respect to the Sun), and thus determines the strength of the asymmetry effect. Variation of the dust production rate on the colatitude α_M can be approximated by a simple cosine function $1 + C^{(1)}(\mu)\cos\alpha_M$, or more generally expanded into the Legendre polynomials. For the initial velocities of the ejected dust particles we take a power-law distribution of the velocity moduli, and a uniform distribution of their vectors inside a cone normal to the surface.

5.2. Phase-space DF

The dust clouds around atmosphereless satellites are completely described with the one-particle phase-space DF $n(\vec{r}, \vec{v})$ of the generated dust cloud. Here we provide a general expression, valid for any initial DF of ejecta $f(\vec{r}_M, \vec{u})$. The derivation of n is based on the transformation of the phase-space variables at the satellite surface along the dust particle trajectories. From the phase-space DF any quantity of interest (number densities, fluxes, etc.) can be calculated.

5.3. Number density

The resulting number density depends on the scaled radius $\tilde{r} = r/r_M$ and the colatitude from the apex of the satellite motion α. The value $n(\tilde{r}, \alpha)$ has been obtained by integrating the phase-space DF over the velocity components. In the particular case of a motionless satellite, our results reduce to those found in PAPER I. When the satellite is moving

the resulting density is an average (spherically symmetric, distance-dependent) value $n^{(\mathrm{symm})}(\tilde{r})$ modulated by a cosine function:

$$n(\tilde{r}, \alpha) = n^{(\mathrm{symm})}(\tilde{r}) \times (1 + C^{(1)}(\mu) \times c_1(\tilde{r}) \times \cos\alpha). \quad (57)$$

The initial asymmetry is given by $C^{(1)}(\mu)$, and then the factor $c_1(\tilde{r})$ describes the propagation of the initial asymmetry to larger distances. Its value at the surface is $c_1(\tilde{r}=1)=1$, and it monotonically decays to a certain constant value as distance increases. Higher accuracy can be achieved by taking into the account higher modes.

5.4. Dependence on the choice of the initial DF

The simple cosine dependence of the number density on the colatitude α is rather robust with respect to changes in the initial DF f (in a physically meaningful range). This result means a very fast decay of higher harmonics of the density field $n(\tilde{r}, \alpha)$ with $\tilde{r}$. We found that only the spherically symmetric (zeroth) mode and the cosine modulation (first harmonic) contribute considerably to the dust cloud configuration.

The spherically symmetric contribution $n^{(\mathrm{symm})}(\tilde{r})$, obtained by averaging the general value $n(r, \alpha)$ over α, depends largely on the initial speed distribution f_u and is almost independent of the angle distribution f_ψ. A weak influence of the angular distribution is perceptible for $r < 1.5 r_M$ only (PAPER I), i.e. very close to the surface of the satellite.

Conversely, the propagation of the initial asymmetry, characterized by $c_1(\tilde{r})$, is only sensitive to the initial distribution of the angles ψ. Different initial DF $f_\psi(\psi)$ result in different asymmetry coefficients $c_1(\tilde{r})$. It turns out, however, that only the mean initial angle $\langle\psi\rangle = \int \psi f_\psi(\psi)\,\mathrm{d}\psi$ is essential. It means that ambiguity of initial $f_\psi(\psi)$ is not of great relevance.

5.5. Applications

Experiments performed by Koschny and Grün (2001a, b) suggest that the mean initial angle $\langle\psi\rangle$ is about 24° (ejection close to the normal of the surface). In that case, the initial asymmetry of the dust production (for any $\mu > 0$) remains persistent over increased radii r. On the other hand, if this angle $\langle\psi\rangle$ is larger than about 45°, the initial asymmetry of the dust cloud vanishes, being, for instance, less than 10% of the initial value $C^{(1)}(\mu)$, for radii $r > 6 r_M$.

A challenging direction of future research would be to search for a leading-trailing asymmetry of the dust clouds around the Galilean moons (through an in-depth analysis of the Galileo dust data), as well as the Saturnian moons (when the Cassini data will become available). Were the asymmetries detected, this would bear further witness to the impact origin of the clouds. Nonetheless, non-detection would not rule out the impact scenario—as we have shown here, lack of asymmetry can be attributed to a wider angular distribution of ejecta.

Fig. 10 shows two representative pictures of the number density field. The trajectory of the spacecraft in this frame would be just a line. Such line could pass at same radial distances regions with different number densities, and total numbers of impact events in the incoming and outgoing leg of the trajectory would be different. This is especially important to test competing dust production scenarios. In this paper, we assumed isotropically distributed interplanetary impactors. However, other families could also matter, such as impactors from planetary system, prograde and retrograde, or interplanetary particles in low-eccentricity and low-inclination orbits. In these cases, the asymmetry axis of the dust production would be different, giving different total numbers of impact events in the incoming and outgoing part of the trajectory. Given the small number of actual impact events detected by Galileo (from few to 10 of impacts per flyby; Krüger et al., 2000, 2003), this integrated effect could allow more reliable statistics over all flybys. Also, different trajectories in Fig. 10a would give different number density slopes and absolute levels. The slopes could become steeper or flatter compared to -2.5 in spherically symmetric case, and absolute levels could be different and dependent on the moon position on the orbit according to the factor $B(\mu)$.

In any case, either detection or non-detection of asymmetries in the data would provide constraints on the angular distribution of ejecta produced by hypervelocity impacts, thereby extending impact experiments from laboratory conditions to real conditions in space, and on the origin and properties of impactors. The results presented here provide necessary theoretical guidelines for a dedicated quest of asymmetries in the data as well as for interpretation of its results.

Acknowledgements

Appendix A. Calculation of the dust production

Taking $b = 1$, dividing Eq. (5) by Eq. (6), substituting velocity modulus v_{imp} from Eq. (2) and resolving the factor $\cos(\vec{r}_M, -\vec{v}_{imp})$, we obtain:

$$\frac{P(\alpha_M)}{P_0} = \frac{1}{\pi} \int \int_{D(\alpha_M, \beta_M)} \sin \alpha_{imp} \, d\alpha_{imp} \, d\beta_{imp}$$

$$\times (1 - 2\mu \cos \alpha_{imp} + \mu^2)$$

$$\times [-\sin \alpha_M \sin \alpha_{imp} \cos(\beta_{imp} - \beta_M)$$

$$-\cos \alpha_M (\cos \alpha_{imp} - \mu)]. \tag{A.1}$$

The domain $D(\alpha_M, \beta_M)$, Eq. (4), is a complicated function of α_M, but the integration can be carried out using different variables. Instead of $(\alpha_{imp}, \beta_{imp})$ we can use other spherical coordinates with respect to $\vec{r}_M$ (instead of $\vec{v}_{moon}$, Table 1 and Fig. 1). The result is

$$\frac{P}{P_0} = \begin{cases} (1 + \mu \cos \alpha_M)^2 \\ \quad \times (1 + \mu^2 + \frac{4}{3}\mu \cos \alpha_M \\ \quad - \frac{2}{3}\mu^2 \cos^2 \alpha_M), & \text{case (a),} \\ \frac{4}{3}\mu(5 + 3\mu^2) \cos \alpha_M, & \text{case (b),} \\ 0, & \text{case (c),} \end{cases} \tag{A.2}$$

where case (a) stands for $\mu \leqslant 1$ or $\mu > 1$ and $\alpha_M \in [\arccos(1/\mu), \pi - \arccos(1/\mu)]$, case (b) for $\mu > 1$ and $\alpha_M \in [0, \arccos(1/\mu)]$ and case (c) for $\mu > 1$ and $\alpha_M \in [\pi - \arccos(1/\mu), \pi]$. Similarly, the solid angle Ω, Eq. (8), is

$$\Omega(\alpha_M) = \begin{cases} 2\pi(1 + \mu \cos \alpha_M), & \text{case (a),} \\ 4\pi, & \text{case (b),} \\ 0, & \text{case (c).} \end{cases} \tag{A.3}$$

Appendix B. Calculation of the number density

Using expression (48) for the initial DF, replacing it in Eq. (38) for the final DF, and calculating the number density [either Eq. (44) or (45)] we have

$$n(\tilde{r}, \alpha) = \frac{N^+ B}{4\pi r_M^2} \frac{1}{\tilde{r}} \sum_i C^{(i)} \int_{\tilde{v}} \int_{\theta} d\tilde{v} \, d\theta \, \frac{\tilde{v} f_{u,\psi}(\tilde{u}, \psi)}{\tilde{u}^2 \cos \psi}$$

$$\times \frac{1}{\pi} \int_0^\pi d\lambda \, \mathbf{P}_i(\alpha_M). \tag{B.1}$$

With $\int_{\tilde{v}} \int_{\theta}$ we denote integration domain for $\tilde{v}$ and θ. The term with $i = 0$ simply reproduces the spherically symmetric result, Eq. (47). Using the addition theorem (Gradshteyn and Ryzhik, 1994)

$$\mathbf{P}_i[\cos \varphi_1 \cos \varphi_2 + \sin \varphi_1 \sin \varphi_2 \cos \lambda]$$

$$= \mathbf{P}_i[\cos \varphi_1] \mathbf{P}_i[\cos \varphi_2]$$

$$+ 2 \sum_{k=1}^{i} \frac{(i-k)!}{(i+k)!} \cos(k\lambda) \mathbf{P}_i^k[\cos \varphi_1] \mathbf{P}_i^k[\cos \varphi_2], \tag{B.2}$$

where $\mathbf{P}_i^k[x]$ are associated Legendre functions of the first kind, and expressing $\cos \alpha_M$ with use of Eq. (34), we can easily integrate over λ (the sum over k vanishes). The result is

$$\frac{1}{\pi} \int_0^\pi d\lambda \, \mathbf{P}_i(\alpha_M) = \mathbf{P}_i(\alpha) \mathbf{P}_i(\Delta\phi). \tag{B.3}$$

Note our notation $\mathbf{P}_i(x) \equiv \mathbf{P}_i[\cos x]$ and that the angle between the launch point and a point along the orbit $\Delta\phi$ does not depend on α and λ. Finally, combining the derived expressions it is easy to verify the resulting Eq. (49).

References

Burchell, M.J., Brooke-Thomas, W., Leliwa-Kopystynski, J., Zarnecki, J.C., 1998. Hypervelocity impact experiments on solid CO_2 targets. Icarus 131, 210–222.

Colwell, J.E., 1993. A general formulation for the distribution of impacts and ejecta from small planetary satellites. Icarus 106, 536–548.

Colwell, J.E., Horányi, M., 1996. Magnetospheric effects on micrometeoroid fluxes. J. Geophys. Res. 101, 2169–2175.

Cuzzi, J.N., Durisen, R.H., 1990. Bombardment of planetary rings by meteoroids—general formulation and effects of Oort Cloud projectiles. Icarus 84, 467–501.

Frisch, W., 1992. Hypervelocity impact experiments with water ice targets. In: Mc-Donnell, J.A.M. (Ed.), Hypervelocity Impacts in Space. University of Kent, Canterbury, Great Britain, pp. 7–14.

Gradshteyn, I.S., Ryzhik, I.M., 1994. Table of Integrals, Series, and Products. Academic Press, San Diego.

Hartmann, W.K., 1985. Impact experiments. 1. Ejecta velocity distributions and related results from regolith targets. Icarus 63, 69–98.

Horányi, M., Burns, J.A., Hamilton, D.P., 1992. The dynamics of Saturn's E ring particles. Icarus 97, 248–259.

Koschny, D., Grün, R., 2001a. Impacts into ice-silicate mixtures: crater morphologies, volumes, depth-to-diameter ratios and yield. Icarus 154, 391–401.

Koschny, D., Grün, R., 2001b. Impacts into ice-silicate mixtures: ejecta mass and size distributions. Icarus 154, 402–411.

Krivov, A.V., Hamilton, D.P., 1997. Martian dust belts: waiting for discovery. Icarus 128, 335–353.

Krivov, A.V., Jurewicz, A., 1999. The ethereal dust envelopes of the Martian moons. Planet. Space Sci. 47, 45–56.

Krivov, A.V., Krüger, H., Grün, E., Thiessenhusen, K.-U., Hamilton, D.P., 2002. A tenuous dust ring of Jupiter formed by escaping ejecta from the Galilean satellites. J. Geophys. Res. 107 (E1), doi: 10.1029/2000JE001434.

Krivov, A.V., Sremčević, M., Spahn, F., Dikarev, V.V., Kholshevnikov, K.V., 2003. Impact-generated dust clouds around planetary satellites: spherically-symmetric case. Planet. Space Sci. 51, 251–269.

Krüger, H., Krivov, A.V., Hamilton, D.P., Grün, E., 1999. Detection of an impact-generated dust cloud around Ganymede. Nature 399, 558–560.

Krüger, H., Krivov, A.V., Grün, E., 2000. A dust cloud of Ganymede maintained by hypervelocity impacts of interplanetary micrometeoroids. Planet. Space Sci. 48, 1457–1471.

Krüger, H., Krivov, A.V., Sremčević, M., Grün, E., 2003. Impact-generated dust cloud surrounding the Galilean moons. Icarus, in press.

Morfill, G.E., Grün, E., Johnson, T.V., 1980. Dust in Jupiter's magnetosphere—origin of the ring. Planet. Space Sci. 28, 1101–1110.

Müller, M., Green, S.F., McBride, N., Koschny, D., Zarnecki, J.C., Bentley, M.S., 2002. Estimation of the dust flux near Mercury. Planet. Space Sci. 50, 1101–1115.

Soter, S., 1971. The dust belts of Mars. Report of Center Radiophysics and Space Research No. 462.

Spahn, F., Thiessenhusen, K., Colwell, J.E., Srama, R., Grün, E., 1999. Dynamics of dust ejected from Enceladus: application to the Cassini dust detector. J. Geophys. Res. 104, 24,111–24,120.

Thiessenhusen, K.-U., Krivov, A., Krüger, H., Grün, E., 2002. Dust envelope of Pluto and Charon. Planet. Space Sci. 50, 79–87.

Weidenschilling, S.J., Davis, D.R., 1986. Oblique impacts: ejecta mass and velocity distributions. Lunar Planet. Sci. XVII, 931–932.

Yamamoto, S., 2002. Measurement of impact ejecta from regolith targets in oblique impacts. Icarus 158, 87–97.

Yamamoto, S., Nakamura, A.M., 1997. Velocity measurements of impact ejecta from regolith targets. Icarus 128, 160–170.